American Mineralogist, Volume 91, pages 1363–1370, 2006

Stacking structure in disordered talc: Interpretation of its X-ray diffraction pattern by using pattern simulation and high-resolution transmission electron microscopy

TOSHIHIRO KOGURE,[1,*] JUN KAMEDA,[1] TOMOYUKI MATSUI,[1] AND RITSURO MIYAWAKI[2]

[1]Department of Earth and Planetary Science, Graduate School of Science, The University of Tokyo, 7-3-1 Hongo, Bunkyo-ku, Tokyo, 113-0033, Japan
[2]Department of Geology, The National Science Museum, 3-23-1 Hyakunin-cho, Shinjuku-ku, Tokyo 169-0073, Japan

ABSTRACT

Stacking structure in disordered talc, $Mg_3Si_4O_{10}(OH)_2$, has been investigated by using high-resolution transmission electron microscopy (HRTEM) and by comparison between experimental and simulated powder X-ray diffraction (XRD) patterns. The talc specimen investigated was massive aggregates of fine platy crystals from the Shirakashi mine, Nagasaki-Prefecture, Japan, formed from regional metamorphism. HRTEM observations revealed that the orientation of the 2:1 layer, which is described by the direction of the lateral shift of $a/3$ from the lower tetrahedral sheet to the upper tetrahedral sheet within the 2:1 layer (intralayer shift), is almost completely disordered. In contrast, lateral displacement between the adjacent tetrahedral sheets across the interlayer region (interlayer displacement) is relatively ordered. The interlayer displacement parallel to the intralayer shift in lower or upper 2:1 layers tends to be avoided.

A Gandolfi camera was used to record XRD patterns from a small fragment of the aggregates, to avoid preferred orientation and artifacts in stacking sequence by grinding. XRD patterns were simulated using the DIFFaX program and compared with experimental patterns. The experimental pattern from $hk = 02$, 11, and $1\bar{1}$ reciprocal lattice rows is explained by a mixture of the stacking sequence with almost random directions of intralayer shift and a small amount of 1*A* dominant stacking sequence. The peak profiles for the reflections indexed with 20*l*, 13*l*, or $1\bar{3}l$ are reproduced by considering their variance, and a slightly different interlayer displacement from that reported in talc-1*A*.

Keywords: Crystal structure, talc, electron microscopy, order-disorder, polytypism, XRD data

INTRODUCTION

The basic structure of talc consists of trioctahedral 2:1 layers with no layer charge and thus, requires a vacant interlayer region. Zvyagin et al. (1969) suggested from electron-diffraction analyses that lateral displacement between the two tetrahedral sheets across the interlayer region of talc is almost $\pm\boldsymbol{a}_i/3$ (i = 1, 2, or 3) where $\pm\boldsymbol{a}_i$ are the vectors connecting the centers of adjacent hexagonal rings in a tetrahedral sheet. They referred to this displacement with a symbol "τ" and is referred to as "interlayer displacement" in the present study. The origin of the interlayer displacement results from the minimization of repulsive forces between the two tetrahedral sheets across the interlayer region (Zvyagin et al. 1969). Later, two X-ray structure analyses were successfully performed for the ordered one-layer polytype (talc-1*A*) (Rayner and Brown 1973; Perdikatsis and Burzlaff 1981). Perdikatsis and Burzlaff (1981) reported that the actual interlayer displacement is $-0.108\boldsymbol{a} + 0.159\boldsymbol{b}$ [$-0.11\boldsymbol{a} + 0.16\boldsymbol{b}$ of Rayner and Brown (1973)]. The magnitude and direction of this vector are $0.297a$ and 8.6° from the $[\bar{1}10]$ direction, respectively, which deviates considerably from the ideal displacement suggested by Zvyagin et al. (1969).

Besides the 1*A* structure, an occurrence of a two-layer monoclinic polytype, talc-2*M* was suggested (Gruner 1934; Hendricks 1938). However, several researchers were doubtful of the existence of talc-2*M* (e.g., Akizuki and Zussman 1978). Furthermore the stacking sequence in disordered talc, which is characterized by broad or extinguished reflections except 00*l*, is not fully understood. The origin of the broad or extinguished reflections can be disorder of orientations in the 2:1 layers (intralayer shift: the lateral displacement from the lower tetrahedral sheet to the upper sheet within the 2:1 layer), which is very common in micas and other phyllosilicates, or disorder of the interlayer displacement, or both.

Because most talc specimens occur as aggregates of fine crystals, powder X-ray diffraction (XRD) is the most convenient technique to investigate its stacking structure. Gualtieri (1999) investigated a disordered talc specimen by comparison between experimental and simulated powder XRD patterns, and suggested a model for the disordered stacking. However, the correspondence between his experimental and simulated patterns is limited and the conclusions are not persuasive. In addition, there is a possibility that grinding specimens for powder XRD measurements may change the original stacking in talc (Pérez-Rodríguez et al. 1988).

Direct observation of the stacking sequence in layered materials by high-resolution transmission electron microscopy (HRTEM) is another method to investigate complicated or disordered stacking sequences. However, HRTEM generally requires a large dose of electrons and some phyllosilicates

* E-mail: kogure@eps.s.u-tokyo.ac.jp

0003-004X/06/0809–1363$05.00/DOI: 10.2138/am.2006.2196

are too beam-sensitive to record HRTEM images of sufficient quality for the determination of the stacking structure. Talc is regarded as one of these phyllosilicates (Veblen and Buseck 1980). However, recently we have successfully determined the stacking structures in phyllosilicates for which it was thought difficult to record HRTEM images (Kogure and Inoue 2005a, 2005b; Kogure et al. 2006).

Because disordered talc possibly has two origins (different intralayer shift and interlayer displacement) for its stacking disorder, HRTEM analysis is critical to distinguish them. However, the use of only HRTEM analysis is not sufficient for the complete understanding of the stacking structure in talc for the following reasons. (1) The area analyzed by HRTEM is very limited and results may not represent the entire specimen. (2) An HRTEM image corresponds to a projection of the atomic arrangement in the specimen along the electron-beam direction. One additional HRTEM image of the same area along another direction is required to understand the stacking sequence completely (Kogure and Nespolo 1999). However this is impossible at present for such beam-sensitive specimens as talc. (3) Precise determination of, for instance, the direction and magnitude of interlayer displacement is not easily determined from HRTEM images owing to limited resolution and distortion by imperfect imaging conditions (astigmatism, misorientation, etc.). To compensate for these problems, it is necessary to construct a model that can quantitatively reproduce experimental XRD patterns, incorporating the information from HRTEM.

In this study, we used the following methods to investigate the stacking structure in talc. (1) HRTEM images of sufficient resolution were recorded to give information about the stacking sequence in talc. (2) XRD patterns were obtained from unground fragments of massive talc by using a Gandolfi camera. (3) Finally, a stacking model that reproduces the experimental XRD pattern was constructed by comparisons between the experimental and simulated patterns, and by HRTEM results.

Samples and methods

The specimen investigated was green-colored massive talc aggregates from the Shirakashi mine, Nagasaki-Prefecture, Japan (a registered specimen of the Geological Survey of Japan, GSJ-M 10986). According to Nishiyama (1990), talc in this area was formed by the reaction between amphibole and CO_2-rich fluid during regional metamorphism. Electron microprobe analysis detected only iron as a secondary component with the Mg/(Mg + ΣFe) atomic ratio being 0.97–0.98. Platy talc crystals of ≤100 μm were preferentially oriented on their (001) plane in a petrographic thin section made from the specimen.

Specimens for TEM examination were prepared from the petrographic thin section. Disks about 3 mm in diameter were cut from the section, and supported on both sides with molybdenum single-hole (1 mm in diameter) disks. Thinning disks to electron transparency was accomplished using argon milling techniques (Fig. 1). HRTEM examination was performed at 200 kV using a JEOL JEM-2010 with a nominal point resolution of 2.0 Å (C_s = 0.5 mm). Degradation in talc by electron radiation is rapid, but not as serious as in kaolin minerals (Kogure and Inoue 2005a). Generally, only one exposure was possible for a view to obtain HRTEM images with magnification of ×400 000 or ×500 000, owing to the radiation damage. Some successful images recorded on films were digitized using a CCD camera for image processing. Noise from amorphous materials on the specimen surfaces was removed using the rotational filtering technique (Kilaas 1998) implemented with Gatan DigitalMicrograph version 2.5 (with respect to the performance of the filtering, see Kogure and Banfield 1998). Multi-slice image simulation was performed using MacTempas (Total Resolution Co.).

A fragment, several hundred micrometers in dimension, was attached to a thin glass fiber for XRD measurements. XRD patterns were obtained with a Gandolfi camera of 114.6 mm in diameter employing Ni-filtered Cu$K\alpha$ radiation. The patterns were recorded on an imaging plate (IP) with an exposure time of about one day. The IP was processed with a Fuji BAS-2500 bio-imaging analyzer with a computer program developed by Nakamuta (1999). Simulation of powder XRD patterns was performed using DIFFaX (version 1.812) (Treacy et al. 1991), which calculates diffraction patterns from layered materials with various stacking sequences.

Results and discussion

Comparison between the experimental XRD pattern and calculated pattern for talc-1*A*

Figure 2 shows an XRD pattern obtained using the Gandolfi camera in the 2θ range from 5 to 70°, and a calculated pattern using structural parameters of talc-1*A* determined by Perdikatsis and Burzlaff (1981) for comparison. The two patterns are considerably different because the data by Perdikatsis and Burzlaff (1981) were obtained from a single crystal, assuming a completely ordered stacking, whereas the Gandolifi pattern is from an aggregate of crystals that may contain extensive stacking disorder. We obtained XRD patterns from two other fragments and confirmed that these patterns are identical, suggesting that the pattern in Figure 2 is representative of the entire specimen. The peak profile for the calculated pattern is a pseudo-Voight function (equal contributions of Gauss and Lorentz functions) with a FWHM (full-width at the half-maximum) of 0.30°, based on the peak width of the basal 00*l* reflections in the experimental pattern.

Ďurovič and Weiss (1983) classified polytypes of talc into two subfamilies, A and B. In subfamily A, the angle between the directions of the adjacent intralayer shift and interlayer displacement is always 0 or ±120°. This scheme can be also applied to disordered stacking sequences, not only ordered polytypes. Reflections indexed with $k = 3n$ (family reflections) are common to polytypes or stacking sequences belonging to the same family

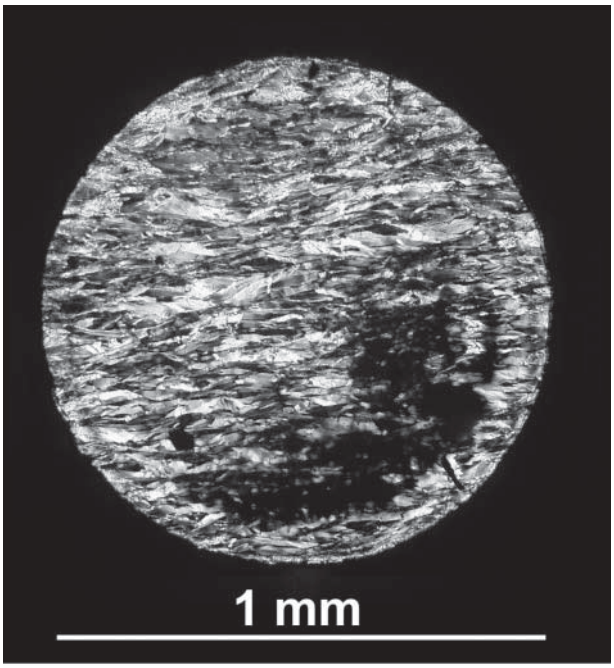

Figure 1. Optical micrograph of the ion-milled TEM specimen. Note that the specimen has a phyllitic texture.

(actually this is not rigorously applied to talc because the interlayer displacement is not exactly $\pm\boldsymbol{a}_i/3$). On the other hand, reflections indexed with $k \neq 3n$ (non-family reflections) are unique for each polytype or stacking sequence within a subfamily. These two types of reflections are considered separately in the experimental XRD pattern in Figure 2.

Except for the basal reflections, the peaks in the 2θ range from 19 to 34° in the calculated pattern correspond to 02*l*, 11*l*, and $\overline{1}1l$ reflections (non-family reflections). In the experimental pattern only one strong peak at 2θ = 19.5° (d = 4.55 Å) with gradual attenuation at higher angles appears in this 2θ range. This pattern is typical of many phyllosilicates with extensive stacking disorder and termed "02,11 band," indicating that reciprocal lattice rows with hk = 02, 11, and $1\overline{1}$ are considerably streaked owing to the stacking disorder. Some weak ripples appear on the peak tail. The positions and intensities of the ripples correspond approximately to those of the peaks in the calculated pattern, implying that domains or crystallites, in which the stacking sequence of 1*A* is dominant, probably exist in the specimen.

The peaks of the type 20*l*, 13*l*, and $1\overline{3}l$ (family reflections) that should occur in a 2θ range of >30° are shown in Figure 3. Note that the peaks for 20*l* appear to be missing in the experimental pattern based on comparison to the calculated pattern. However, further examination suggests that they are not of zero intensity, but they are shifted to form shoulders on the broad peaks corresponding to 13*l* and $1\overline{3}l$. Although the peak positions are not coincident, the intensity distribution for these reflections is similar to that in the calculated pattern for talc-1*A*. This indicates that the stacking sequences in the specimen predominantly belong to subfamily A (note that talc-1*A* belongs to subfamily A). In other words, the angle between the directions of the adjacent intralayer shift and interlayer displacement is always 0 or ±120°.

HRTEM examination of stacking sequences in talc

Figure 4a shows the crystal structure and simulated HRTEM contrast for talc-1*A* along the three directions ([100], [110], and [$1\overline{1}0$]), using atomic parameters reported by Perdikatsis and Burzlaff (1981). The distinctive dark spots in the contrast, one of which corresponds to a pyroxene-like tetrahedral chain along the beam direction in a tetrahedral sheet, provide the essential information for the stacking sequence. According to Baronnet (1992), three directions of staggers (no stagger, stagger to the right, and stagger to the left) from the spots at the lower tetrahedral sheet to those at the upper tetrahedral sheet within the 2:1 layer, which originate in the intralayer shift, are expressed with "0", "+," and "–", respectively. The stagger of the spots across the interlayer region, which originates in the interlayer displacement, is depicted similarly (Fig. 4a). Figure 4b shows an experimental HRTEM image with the staggers derived from the contrast. In the ideal case with the displacement of $\pm\boldsymbol{a}_i/3$ (Zvyagin et al. 1969; Ďurovič and Weiss 1983), the magnitude of stagger at "0", "+," and "–" is zero, +b/6, and –b/6, respectively. However, the magnitudes of the stagger at the interlayer region in the calculated and experimental contrasts deviate from these ideal values. For instance, the magnitude of stagger at the interlayer region with "0" is not exactly zero (the spots at the two sheets are not vertically aligned exactly), because the amount of the actual interlayer displacement is shorter than $a/3$ and the direction of the displacements deviates from $\pm\boldsymbol{a}_i/3$, as discussed above. Although the actual magnitude and direction of the interlayer displacement possibly can be estimated from this deviation in experimental images, this is difficult because HRTEM contrast is distorted by imperfections in imaging (astigmatism, misorentation, etc.). In the present study, we use HRTEM images only to distinguish the three directions for intralayer shift and interlayer displacement with the assumption that all stacking sequences belong to subfamily A.

Figure 5 shows an HRTEM image where the staggers of intralayer shift and interlayer displacements for more than 80 layers in a crystal were determined successfully. The following results are derived from the image. (1) The direction of intralayer shift is almost completely disordered whereas the + direction of interlayer displacement is dominant, as shown in the table in the bottom left. (2) The same direction for adjacent intralayer shift and interlayer displacement tends to be avoided. Indeed, there is no sequence where the directions of interlayer displacement and those of intralayer shift below and above the interlayer

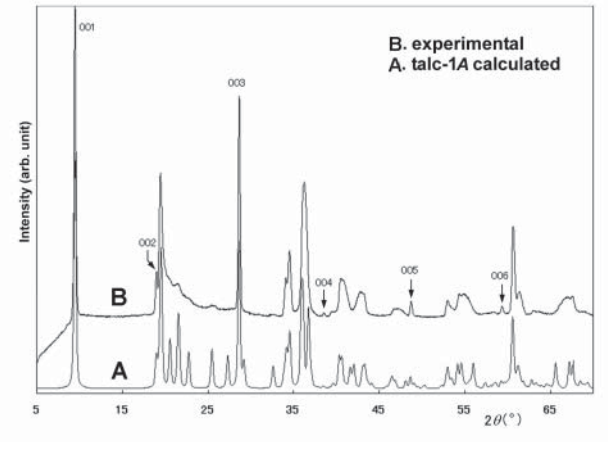

FIGURE 2. Calculated XRD pattern (A) for talc-1*A* using DIFFaX and experimental pattern (B) obtained from a fragment of the specimen using a Gandolfi camera. The peak profile for the calculated pattern is a pseudo-Voight function with a FWHM of 0.30°.

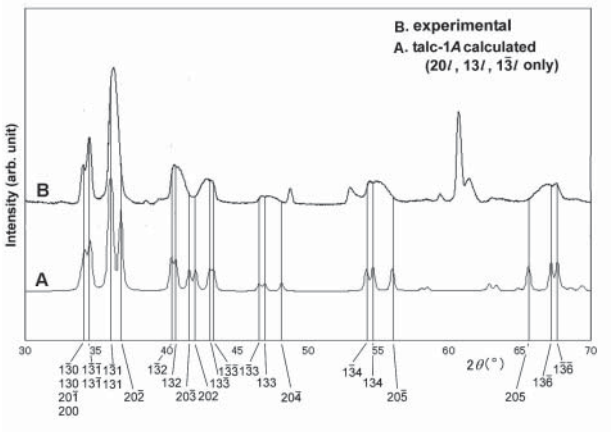

FIGURE 3. Calculated pattern (A) using reflections with hk = 20, 13, and $1\overline{3}$ for talc-1*A* and the experimental pattern (B).

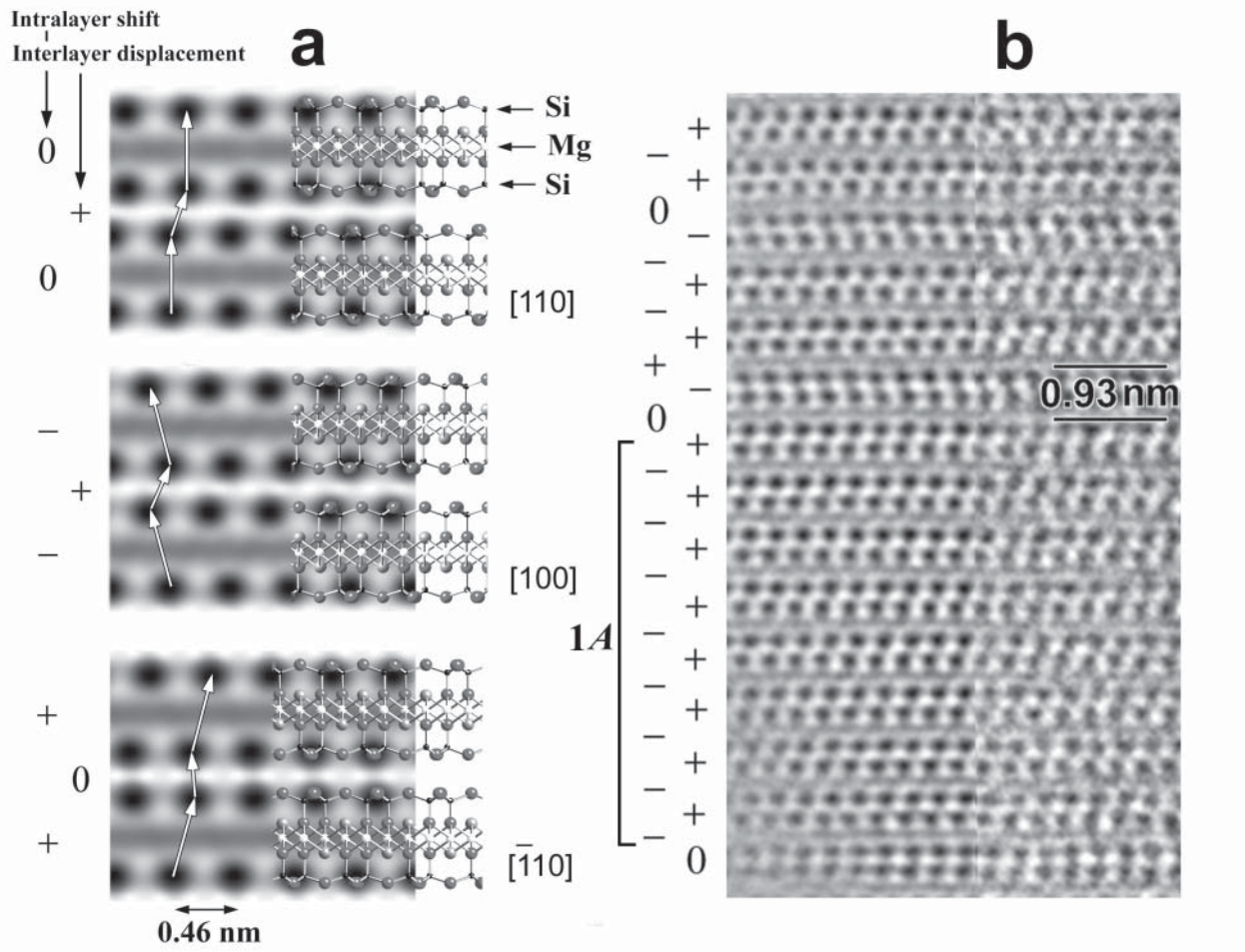

FIGURE 4. (**a**) Crystal structure and multi-slice computer simulation for the HRTEM contrasts of talc-1*A* along three directions. The parameters for the simulation are as follows. Specimen thickness 2.5 nm; defocus –40 nm; acceleration voltage 200 kV; spherical aberration coefficient (C_s) 0.5 mm; spread of focus; 10 nm. The white arrows connect the closest dark spots between the adjacent tetrahedral sheets, and slant of the arrows represents the stagger direction. The characters ("0", "+," and "–") on the left of the image indicate the stagger directions between the two tetrahedral sheets within the 2:1 layer (the left column) and those across the interlayer region (the right column). The former originates in the intralayer shift and the latter in the interlayer displacement. (**b**) An HRTEM image of the specimen. The right side is the raw image and the left side is the filtered image. The region with ordered 1*A* stacking is observed in **b**.

region are the same (see the table in the bottom right). The first result contrasts with pyrophyllite (Kogure et al. 2006) where intralayer shift was nearly ordered but interlayer displacement is heavily disordered. This difference between pyrophyllite and talc is probably related to the degree of corrugation of the basal oxygen planes on the surface of the 2:1 layer. In pyrophyllite, the silicon tetrahedra are considerably tilted to form the large octahedral vacancy sites in the dioctahedral sheet, which results in the distinctive corrugation of the basal oxygen plane (Evans and Guggenheim 1988). Because this corrugation is parallel to the intralayer shift of the 2:1 layer, the ordering of intralayer shift is probably favored by decreasing the interlayer distance with minimum oxygen-oxygen repulsion. On the other hand, such corrugation does not exist in talc with a trioctahedral 2:1 layer (Evans and Guggenheim 1988). Hence, different intralayer shift between adjacent layers in talc do not significantly change the atomic configuration at the interlayer region. In contrast, it is difficult to explain why the direction of interlayer displacement tends to be ordered in the present specimen. One possibility is that shear stress during crystal growth ordered the interlayer displacement in a certain direction. As shown in Figure 1, platy talc crystals in the aggregates are oriented to form a phyllitic texture. Shear stress applied to the rock may have formed the phyllitic texture and also ordered the interlayer displacement in the crystals.

The second result is similar to that in pyrophyllite (Kogure et al. 2006). In pyrophyllite, interlayer displacement in the same direction as the intralayer shift below and/or above the interlayer region is not favorable owing to the surface corrugation of the pyrophyllite layer. Because such surface corrugation does not exist in the trioctahedral 2:1 layer, probably other explanations are required for talc.

Simulation of XRD patterns by DIFFaX

Finally the stacking structure has been evaluated by comparing the experimental XRD pattern and simulated pattern calculated by DIFFaX, incorporating the HRTEM results. First, the pattern in the 2θ range from 19 to 34° (02, 11 band) is simulated. As shown in the HRTEM result (Fig. 5), the direction of the interlayer displacement is generally ordered. Therefore, we do not consider the disorder of the interlayer displacement in the simulation. In contrast, the direction of the intralayer shift is heavily disordered in the specimen. Therefore, three types of 2:1 layers (layers 1, 2, and 3) that are rotated by ±120° with respect to one another are included in the calculation. The direction of the interlayer displacement is set to be parallel to the intralayer shift in layer 3. The transition probability that layer *i* is succeeded by layer *j* is expressed as α_{ij} and the stacking sequence is expressed by a 3 × 3 matrix of α_{ij} (Treacy et al. 1991).

The result of the simulation using various sets of α_{ij} is shown with the experimental pattern in Figure 6. Pattern A in the figure is the result with all α_{ij} set at 1/3, i.e., stacking of the three layers is random. The simulated pattern has a sharp peak at 2θ = 19.5° (d = 4.55 Å) and smooth tail from the peak at higher angles. This profile roughly reproduces the experimental pattern except for the weak ripples on the tail. Next, from the HRTEM examination (Fig. 5), we modified the matrix such that the transition probability for layer 3 to succeed layer 3 (α_{33}) is zero (Pattern B). The ratio between the number of layers 1, 2, and 3 expected from this matrix is 3:3:2 (See Appendix). The simulated pattern shows some weak ripples on the tail, which approximately resemble the experimental pattern, but the correspondence is not complete. We also set α_{13} and α_{23} to be 2/3 of α_{11}, α_{21}, α_{12}, and α_{22}, and α_{33} was set to zero (Pattern C, see also the table in the figure). The ratio of the three layer types expected from this matrix is 2:2:1, which is nearly equal to the ratio observed in Figure 5. However, the modulation of the tail obviously does not resemble that of the experimental pattern.

As indicated above, the positions and intensities of the ripples in the experimental pattern nearly correspond to those of the peaks for talc-1*A*. Therefore, domains or crystallites may exist with the 1*A* stacking sequence dominant, in addition to those with the disordered stacking sequence. Although the stacking sequence in Figure 5 shows no tendency for adjacent layers to have the same orientation, other HRTEM images indicated

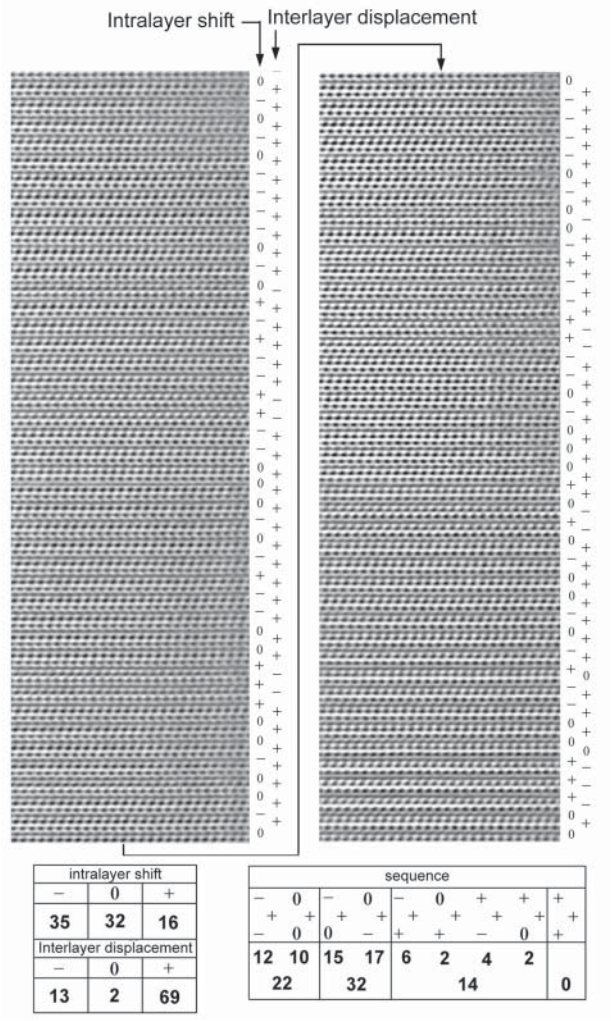

FIGURE 5. Filtered HRTEM image of the talc specimen and determined stagger directions corresponding to the intralayer shift and interlayer displacement in individual layers. The list in the bottom-left shows the number of three stagger directions observed in the figure. The list in the bottom-right shows the number of stacking sequences for adjacent two layers where the stagger direction of the interlayer displacement at the interlayer region is "+."

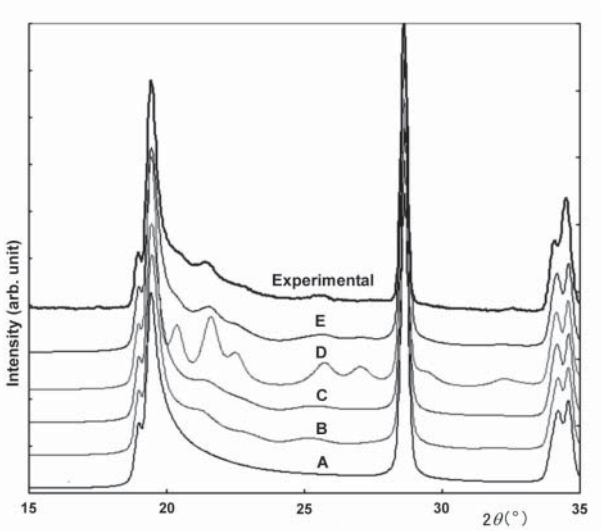

	α_{11}	α_{12}	α_{13}	α_{21}	α_{22}	α_{23}	α_{31}	α_{32}	α_{33}
A	1/3	1/3	1/3	1/3	1/3	1/3	1/3	1/3	1/3
B	1/3	1/3	1/3	1/3	1/3	1/3	1/2	1/2	0
C	3/8	3/8	1/4	3/8	3/8	1/4	1/2	1/2	0
D	4/5	1/5	0	4/5	1/5	0	1/2	1/2	0

FIGURE 6. Several simulated XRD patterns of disordered talc, using three orientations of the 2:1 layers (layers 1, 2, and 3) and the same interlayer displacement (see the text). The transition probabilities, α_{ij}, for the simulated patterns A, B, C, and D are shown in the table. Pattern E is the mixture of patterns C (85%) and D (15%), and the uppermost pattern is the experimental pattern for comparison.

stacking sequences where 1*A* is dominant, as shown in the lower part of Figure 4b. Pattern D is a simulation using α_{ij} corresponding to a 1*A*-dominant sequence (see the table in the figure). The pattern has peaks where their position and intensity are similar to those for 1*A* but the peak widths are broadened. If Patterns C and D are mixed with a ratio of 85:15, then Pattern E is produced, which closely approximates the experimental pattern. This solution is not unique and it is possible that other models could be derived that reproduce the experimental pattern. It is obvious that more detailed or quantitative discussion is difficult using only the powder XRD pattern.

Next, peaks in the 2θ range from 34 to 70° (Fig. 3), most of which are family reflections, were simulated. It is likely that the origin of the discrepancy between the experimental peaks for family reflections and calculated peaks for talc-1*A* (Fig. 3) is related to different interlayer displacements. The interlayer displacement between the two layers with different intralayer shifts may not be the same as that for talc-1*A*. Hence, "averaged" interlayer displacements for the disordered stacking sequence can deviate from that of talc-1*A*. As discussed above, the interlayer displacement in talc-1*A* obtained by Perdikatsis and Burzlaff (1981) is $-0.108\boldsymbol{a} + 0.159\boldsymbol{b}$, which deviates considerably from the ideal displacement (see Fig. 7b). Because of this deviation, the three reciprocal lattice nets (20*l*, 13*l*, and $1\bar{3}l$) are not identical, and corresponding reflections (e.g., 205, $13\bar{6}$, and $1\bar{3}6$ in pattern A in Fig. 3) are split. If the displacement is ideal ($-\boldsymbol{a}/6 + \boldsymbol{b}/6$), these three reflections superimpose to form an apparent single peak (Pattern B in Fig. 7a). The amount of this split in the experimental pattern appears to be smaller than that for talc-1*A*. This suggests that the interlayer displacement in the specimen is between the ideal displacement and that for 1*A*. Pattern C is a simulation where the observed peak positions are best modeled by the optimization of the interlayer displacement (Fig. 7b).

The main remaining discrepancy between Pattern C and the experimental pattern is peak width. The peak width in the experimental pattern is considerably varied between individual peaks. For instance, the peaks for the 20*l* reflections appear considerably broader than others. This result implies that the peak broadening is not explained by a short coherent length related to the grain size, etc. As noted above, the interlayer displacement can be different between individual interlayer regions, depending on the intralayer shifts below and above the regions. Thus, interlayer displacement can have a variance, besides the averaged value. This variance can be incorporated into the calculation by using "a set of anisotropic layer-stacking uncertainty parameters," B_{mn} (m, n = 1, 2, or 3), in DIFFaX (Treacy et al. 1991).[1] These coefficients act in the same way as anisotropic thermal displacement parameters for atom positions, usually determined by X-ray structure analyses. Because the variance of the interlayer displacement can be expressed as an ellipse on the (001) plane, B_{11}, B_{22}, and B_{12} require optimization with the other coefficients (B_{33}, B_{23}, and B_{31}) set to zero. Pattern D is a simulated result with optimized B_{mn} (B_{11} = 4.8, B_{22} = 3.2, and B_{12} = –0.6 Å^2), which reproduces the experimental pattern well. The corresponding ellipse that represents the variance (mean displacement) of the interlayer displacement is shown in Figure 7b. The ellipse covers the interlayer displacement of 1*A* and the ideal displacement.

Finally, comparison between the calculated pattern with the optimized parameters described above (those for Pattern E in Fig. 6 and for Pattern D in Fig. 7), and the experimental pattern for a 2θ range of 5 to 85° is shown in Figure 8. Correspondence between the two patterns is sufficiently acceptable. The development of a program containing a *least-squares* method to optimize parameters more quickly and precisely may lead to a slightly better result.

[1] For the simulation using B_{mn}, version 1.812 of DIFFAX should be used, as previous versions did not recognize minus values for B_{mn}.

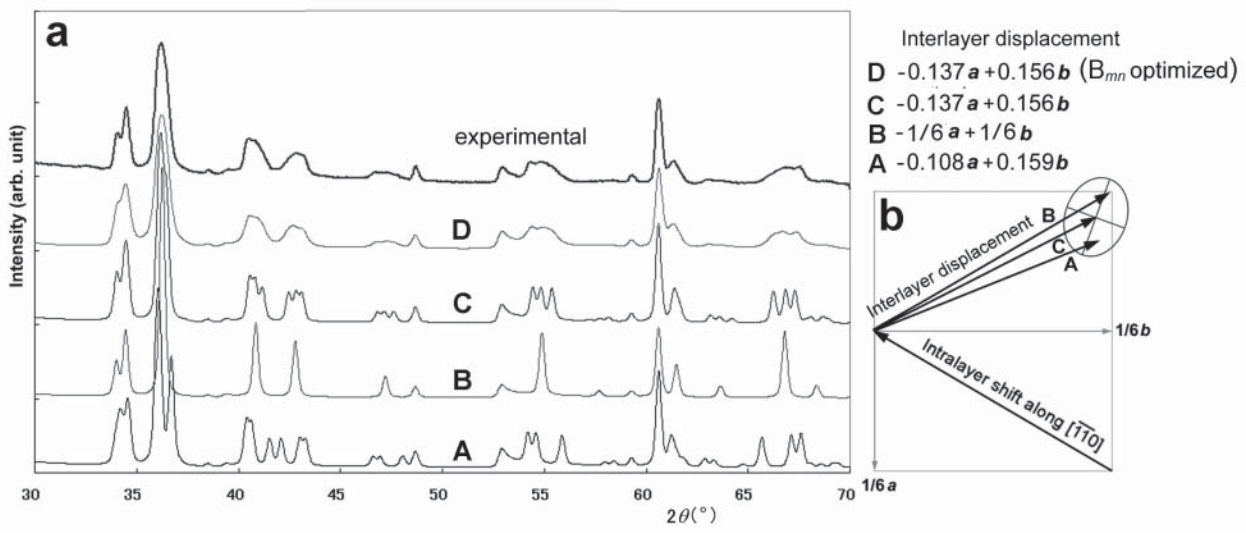

FIGURE 7. (**a**) Simulated XRD patterns in the 2θ range from 30 to 70° with various interlayer displacements, and the experimental pattern for comparison. (**b**) Vectors that represent the interlayer displacement used for the simulated patterns and the ellipse that represents anisotropic layer stacking uncertainty parameters (B_{mn}) used for the calculation of pattern D.

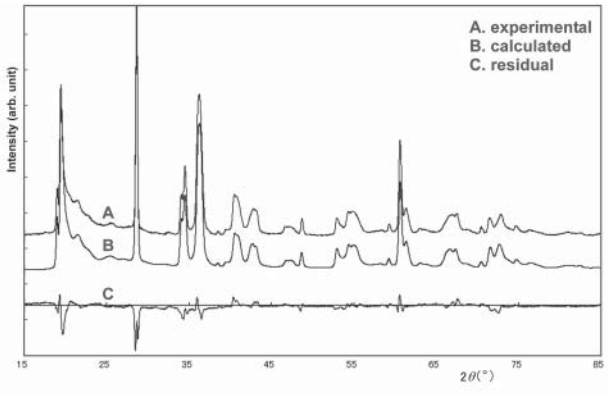

FIGURE 8. Comparison between the final simulated and experimental XRD pattern in 2θ range from 5 to 85°.

Our conclusions for the stacking structure in disordered talc are different from those previously suggested by Gualtieri (1999), who also considered a comparison between experimental and simulated X-ray diffraction patterns. He attributed the origin of the disorder to the various directions and magnitudes of interlayer displacement. However, the correspondence between the experimental and calculated patterns in his result (Fig. 9 in Gualtieri 1999) is poor, especially in the 2θ range from 20 to 30°. Also, he made comparisons only to 2θ = 45°. Furthermore, several peaks appear between the 001 and 002 peaks in his simulation to see the effect of disorder of intralayer shift or layer rotation (Fig. 6 in Gualtieri 1999), which suggests an error in the simulation. We note, however, that our specimen differs from his, which may derive different results in the two studies.

In the present study, several new techniques to investigate the stacking structure in disordered talc were introduced, in particular the combination of HRTEM and powder XRD (including its simulation). XRD patterns obtained using a Gandolfi camera produced patterns without preferred orientation and distortions by grinding. The nature of stacking disorder in other phyllosilicates and layered materials may be better understood, by applying these methods.

ACKNOWLEDGMENTS

We are grateful to Y. Banno (Geological Survey of Japan, AIST) for donating the talc specimen. We thank M.J. Treacy (Arizona State University) for discussions about DIFFaX and improvements of the program. We also thank V.A. Drits (Russian Academy of Sciences), S. Guggenheim (University of Illinois at Chicago), J.E. Post (Smithsonian Institution), and H. Dong (Miami University) for their comments on the manuscript. We express our appreciation to T. Takeshige (the University of Tokyo) for preparation of the TEM specimens. Transmission electron microscopy was performed in the Electron Microbeam Analysis Facility of Department of Earth and Planetary Science, University of Tokyo. This work was partly supported by a Grant-in-Aid No. 17340160 [Section (B)] by the Japan Society for the Promotion of Science (JSPS).

REFERENCES CITED

Akizuki, M. and Zussman, J. (1978) The unit cell of talc. Mineralogical Magazine, 42, 107–110.

Baronnet, A. (1992) Polytypism and stacking disorder. In P. Buseck, Ed., Minerals and reactions at the atomic scale: Transmission electron microscopy, 27, p. 231–288. Reviews in Mineralogy, Mineralogical Society of America, Chantilly, Virginia.

Ďurovič, S. and Weiss, Z. (1983) Polytypism of pyrophyllite and talc. Part I. OD interpretation and MDO polytypes. Silikáty, 27, 1–18.

Evans, B.W. and Guggenheim, S. (1988) Talc, pyrophyllite, and related minerals. In S.W. Bailey, Ed., Hydrous Phyllosilicates (exclusive of micas), 19, p. 225–294. Reviews in Mineralogy, Mineralogical Society of America, Chantilly, Virginia.

Gualtieri, A.F. (1999) Modelling the nature of disorder in talc by simulation of X-ray powder patterns. European Journal of Mineralogy, 11, 521–532.

Gruner, J.W. (1934) The crystal structure of talc and pyrophyllite. Zeitschrift für Kristallographie, 88, 412–419.

Hendricks, S.B. (1938) The crystal structure of talc and pyrophyllite. Zeitschrift für Kristallographie, 99, 264–274.

Kilaas, R. (1998) Optical and near-optical filters in high-resolution electron microscopy. Journal of Microscopy, 190, 45–51.

Kogure, T. and Banfield, J.F. (1998) Direct identification of the six polytypes of chlorite characterized by semi-random stacking. American Mineralogist, 83, 925–930.

Kogure, T. and Inoue, A. (2005a) Determination of defect structures in kaolin minerals by High-Resolution Transmission Electron Microscopy (HRTEM). American Mineralogist, 90, 85–89.

——— (2005b) Stacking defects and long-period polytypes in kaolin minerals from a hydrothermal deposit. European Journal of Mineralogy, 17, 465–473.

Kogure, T. and Nespolo, M. (1999) First occurrence of a stacking sequence with (±60°, 180°) rotation in Mg-rich annite. Clays and Clay Minerals, 47, 784–792.

Kogure, T., Jige, M., Kameda, J., Yamagishi, A., Miyawaki, R., and Kitagawa, R. (2006) Stacking structures in pyrophyllite revealed by high-resolution transmission electron microscopy (HRTEM). American Mineralogist, 91, 1293–1299.

Nakamuta, Y. (1999) Precise analysis of a very small mineral by an X-ray diffraction method. Journal Mineralogical Society of Japan, 28, 117–121 (in Japanese with English abstract).

Nishiyama, T. (1990) CO_2-metasomatism of a metabasite block in a serpentine melange from the Nishisonogi metamorphic rocks, southwest Japan. Contributions to Mineralogy and Petrology, 104, 35–46.

Perdikatsis, B. and Burzlaff, H. (1981) Strukturverfeinerng am Talk $Mg_3[(OH)_2Si_4O_{10}]$. Zeitschrift für Kristallographie, 156, 177–186 (in German).

Pérez-Rodríguez, J.L., Nadrid Sánchez del Villar, L., and Sánchez-Soto, P.J. (1988) Effects of dry grinding on pyrophyllite. Clay Minerals, 23, 399–410.

Rayner, J.H. and Brown, G. (1973) The crystal structure of talc. Clays and Clay Minerals, 21, 103–114.

Treacy, M.M.J., Newsam, J.M., and Deem, M.W. (1991) A general recursion method for calculating diffracted intensities from crystals containing planar faults. Proceedings of the Royal Society of London A, 433, 499–520.

Veblen, D.R. and Buseck, P.R. (1980) Microstructures and reaction mechanisms in biopyriboles. American Mineralogist, 65, 599–623.

Zvyagin, B.B., Mishchenko, K.S., and Soboleva, S.V. (1969) Structure of pyrophyllite and talc in relation to the polytypes of mica-type minerals. Soviet Physics—Crystallography, 13, 511–515.

MANUSCRIPT RECEIVED DECEMBER 21, 2005
MANUSCRIPT ACCEPTED APRIL 10, 2006
MANUSCRIPT HANDLED BY STEPHEN GUGGENHEIM

APPENDIX. PROBABILITY OF EACH LAYER TYPE AT THE n^{TH} LAYER

The probability $[p_j^{(n)}]$ that the n^{th} layer ($n > 1$) from the bottom of a crystal is layer-type j is expressed using the transition probabilities (α_{ij}) and the probabilities $[p_j^{n-1}]$ for the preceding layer as,

$$p_j^{(n)} = \sum_i \alpha_{ij} p_i^{(n-1)}$$

Hence, if we give the probability $[p_j^{(1)}]$ of each layer-type for the first layer, then the probabilities for all layers can be calculated by this equation. For example, we used the following α_{ij} for the DIFFaX simulation in the above discussion as:

$\alpha_{11} = \alpha_{12} = \alpha_{13} = \alpha_{21} = \alpha_{22} = \alpha_{23} = 1/3$, $\alpha_{31} = \alpha_{32} = 1/2$, $\alpha_{33} = 0$

If the probabilities for $p_j^{(1)}$ are given as $p_1^{(1)} = p_2^{(1)} = p_3^{(1)} = 1/3$, then the probabilities of layer-type j for each layer can be calculated numerically, as follows.

n^{th} layer	$p_1^{(n)}$	$p_2^{(n)}$	$p_3^{(n)}$
1	1/3	1/3	1/3
2	0.3888	0.3883	0.2222
3	0.3703	0.3703	0.2592
4	0.3764	0.3764	0.2468
5	0.3743	0.3743	0.2509
6	0.3750	0.3750	0.2495
7	0.3747	0.3747	0.2500
8	0.3748	0.3748	0.2498
9	0.3747	0.3747	0.2498
10	0.3747	0.3747	0.2498

The calculated probability in each row quickly converges to a specific value. Although the general derivation of these convergent values is difficult, they can be derived in this case as follows:

Because $\alpha_{13} = \alpha_{23}$ and $\alpha_{33} = 0$,

$$p_3^{(2)} = \alpha_{13}p_1^{(1)} + \alpha_{23}p_2^{(1)} + \alpha_{33}p_3^{(1)} = \alpha_{13}(p_1^{(1)} + p_2^{(1)})$$
$$= \alpha_{13}(1 - p_3^{(1)}) = \alpha_{13} - \alpha_{13}p_3^{(1)}$$

$$p_3^{(3)} = \alpha_{13} - \alpha_{13}p_3^{(2)} = \alpha_{13} - \alpha_{13}(\alpha_{13} - \alpha_{13}p_3^{(1)}) = \alpha_{13} - \alpha_{13}^2 + \alpha_{13}^2 p_3^{(1)}$$

$$p_3^{(4)} = \alpha_{13} - \alpha_{13}^2 + \alpha_{13}^3 - \alpha_{13}^3 p_3^{(1)}$$

.....

$$p_3^{(n)} = \sum_{i=1}^{n-1} (-1)^{i-1}\alpha_{13}^i + (-1)^{n-1}\alpha_{13}^{n-1}p_3^{(1)}$$
$$= \alpha_{13}/(1+\alpha_{13}) + (-1)^{n-1}\alpha_{13}^{n-1}p_3^{(1)}$$

If α_{13} (= α_{23}) does not closely approximate one, the second term in this equation rapidly decreases. Then the first term expresses the convergent value for $p_3^{(n)}$. If $\alpha_{13} = \alpha_{23} = 1/3$, $p_3^{(n)}$ converges to 1/4. In the present case, as $\alpha_{j1} = \alpha_{j2}$, the convergent values for layer-types 1 and 2 should be equal. They are

$$p_1^{(n)} = p_2^{(n)} = (1 - p_3^{(n)})/2 = 3/8.$$

As a consequence, the ratio of the three convergent values ($p_3^{(n)}$:$p_2^{(n)}$:$p_3^{(n)}$) is 3:3:2.